TRANSLATIONAL RESEARCH
IN VETERINARY SCIENCE

Vol. 9, No. 2, 2026

ISSN 2657-4489 (online)

Biogenic silver-nanocomposite-modified two-layer concrete paving blocks: fabrication routes and physicochemical characterization

Marzena Zawadzka[1,2] ,Viorica Railean[1,3*], Dariusz Buchaniec[2], Paweł Pomastowski[1]

[1] Institute of Advanced Studies, Nicolaus Copernicus University in Toruń, 4 Wileńska Street, 87-100 Toruń, Poland

[2] College of Technical Sciences, WSG University, 2 Garbary Street, 85-229 Bydgoszcz, Poland

[3] Department of Infectious and Invasive Diseases and Veterinary Administration, Institute of Veterinary Medicine, Nicolaus Copernicus University in Toruń, 13 Szosa Bydgoska Street, 87-100 Toruń, Poland

* Corresponding author: viorica.railean@umk.pl

DOI: https://doi.org/10.12775/TRVS.2026.002

Abstract

Two-layer concrete paving blocks provide a practical architecture for concentrating functional additives within the exposed facing layer while retaining a conventional structural base. This study evaluated four routes for introducing a previously characterized biogenic silver nanocomposite, designated AgNP, into or onto the facing layer. Five formulations were prepared: an unmodified control (CTRL), surface spraying with a 6.67 mg mL^{-1} AgNP suspension (AgNP-S), surface powder dusting (AgNP-PD), incorporation of the AgNP suspension into the facing mixture at 0.41 wt% relative to cement (AgNP-SI), and solution incorporation followed by powder dusting (AgNP-SI+PD). AgNP-SI was selected for detailed comparison with CTRL because it combined a macroscopically uniform surface with a defined incorporated dose. Morphology and elemental distribution were examined by scanning electron microscopy coupled with energy-dispersive X-ray spectroscopy (SEM-EDS), whereas matrix-level chemical features were evaluated by Fourier-transform infrared (FTIR) and Raman spectroscopy. Both CTRL and AgNP-SI displayed heterogeneous aggregate and hydration-product morphologies, with no gross disruption of the cementitious matrix in the analyzed fields. EDS mapping confirmed silver retention in AgNP-SI and revealed a heterogeneous distribution containing Ag-rich microdomains. The software-reported mean for selected modified microareas was 4.33 mass% Ag, while point spectra ranged from 0.48 to 22.14 mass% Ag; these values represent local semiquantitative microanalysis rather than bulk composition. FTIR spectra retained the principal silicate, carbonate, and hydration-product bands. Raman spectra of AgNP-SI showed intensified features near 1350cm^{-1}, and 1590–1600cm^{-1}, consistent with carbonaceous components of the biogenic coating and a possible local Ag-associated enhancement of scattering. Collectively, the results demonstrate that the biogenic silver-bearing phase can be selectively incorporated into the wearing layer and remains analytically detectable without gross alteration of the dominant cementitious framework.

Highlights

- A biogenic silver nanocomposite was localized exclusively within the exposed facing layer of two-layer paving blocks.

- Four application routes were compared: spraying, powder dusting, suspension incorporation, and a combined route.
- Suspension incorporation at 0.41 wt% relative to cement yielded the most macroscopically homogeneous modified surface.
- SEM-EDS confirmed retained silver and spatially heterogeneous Ag-rich microdomains in AgNP-SI.
- FTIR preserved the dominant cementitious fingerprint, whereas Raman revealed AgNP-associated carbonaceous features.

Keywords: biogenic silver nanocomposite; silver nanoparticles; cementitious composite; two-layer paving block; facing layer; SEM-EDS; FTIR; Raman spectroscopy; livestock-facility surfaces

Abbreviations: AgNP, biogenic silver nanocomposite containing silver nanoparticles; AgNP-S, surface-sprayed specimen; AgNP-PD, powder-dusted specimen; AgNP-SI, suspension-incorporated specimen; AgNP-SI+PD, suspension-incorporated and powder-dusted specimen; C-S-H, calcium-silicate-hydrate; CTRL, unmodified control; EDS, energy-dispersive X-ray spectroscopy; FTIR, Fourier-transform infrared spectroscopy; SEM, scanning electron microscopy; w/c, water-to-cement ratio.

1. Introduction

Biosecurity in modern livestock production is intrinsically multilayered because infectious agents can enter or circulate through animals, personnel, footwear, clothing, equipment, vehicles, feed, water, and repeatedly contaminated environmental interfaces [1], [2]. Entry thresholds, changing zones, service corridors, and loading areas are especially important because they concentrate traffic between epidemiological compartments. Experimental and field observations have implicated boots, coveralls, and related fomites in the mechanical transfer of porcine viruses [3], [7], while African swine fever and avian influenza continue to require rigorous cleaning, disinfection, movement control, and separation of clean and contaminated zones [4], [5], [6]. These findings support an integrated barrier concept rather than reliance on any single hygienic intervention [1]–[7].

Disinfectant mats and footbaths are widely used at livestock-facility access points because they are inexpensive and operationally visible [3], [5], [6]. Their effectiveness nevertheless depends on prior removal of gross contamination, maintenance of the active-substance concentration, complete wetting, adequate contact time, timely renewal, and consistent user compliance [3]–[6]. Organic matter from manure, litter, and soil can consume disinfectants or shield microorganisms, while brief passage through a bath may limit the effective exposure period. A permanently installed functional surface could therefore complement scheduled sanitation by presenting an active material directly at the traffic interface within a broader biosecurity system.

Two-layer concrete paving blocks are well suited to this concept because the structural base can provide mechanical support, whereas a thinner facing layer can concentrate a functional additive close to the exposed surface. This architecture reduces the amount of modifier required relative to full-volume incorporation and enables the application route to be treated as a design variable. Studies of nanoparticle-functionalized cementitious materials show that functional performance is governed not only by nominal dose but also by dispersion, agglomeration, hydration, pore-solution chemistry, surface roughness, porosity, and retention during service [8]–[11]. Surface deposition may maximize immediate accessibility, whereas incorporation into the cementitious phase can promote physical retention and a more continuous spatial distribution.

Silver nanoparticles are among the most extensively investigated antimicrobial nanomaterials. Their biological activity reflects coupled particle-surface interactions, partial oxidation, dissolution, and the action of released

Ag^+ species [12], [13], [15], [16], [18]–[21], [24], [25], [27]–[29]. Reported mechanisms include adsorption to cell envelopes, membrane destabilization, protein-thiol binding, respiratory-chain disruption, oxidative stress, nucleic-acid damage, and interference with biofilm formation [12], [13], [15], [16], [24], [25]. Activity depends strongly on particle shape and size [14], oxidation state [16], storage-dependent dissolution [20], ion-release kinetics [21], capping chemistry [26], aggregation, and medium composition [18], [19], [25]. The possibility of reduced bacterial susceptibility under sustained silver selection has also been demonstrated [22], [23]. The modifier used in the present study was a biogenic silver nanocomposite previously synthesized with *Lactobacillus paracasei* isolated from whey; it comprised metallic silver cores averaging approximately 18 ± 2.4 nm and an associated organic biomolecular coating [17].

Silver has been introduced into cementitious materials by direct incorporation, surface treatment, and hybrid photocatalytic routes [8]–[11], [30]–[33]. Noeiaghaei et al. [8] demonstrated that nanoparticle surface treatment can inhibit bacterial growth on cemented materials, whereas Ceran et al. [9] showed that dispersed AgNP additions generally provide more favorable composite behavior than powdered additions when agglomeration is controlled. Silver-containing surface nanocoatings are also sensitive to substrate roughness and porosity [10], and broader reviews identify dose, dispersion, and matrix compatibility as central parameters in antimicrobial concrete design [11]. AgNP-modified calcium-silicate cements [30], Ag-modified TiO_2 cementitious systems [31], nanosilver-modified concrete [32], and Portland cement impregnated with colloidal AgNPs [33] further demonstrate the feasibility of integrating silver-bearing phases with inorganic binders. However, the relationship between application route, silver localization, and matrix-level physicochemical response has not been established for a two-layer paving unit containing a biogenic Ag nanocomposite.

Accordingly, this study aimed to fabricate two-layer concrete paving blocks in which the biogenic Ag nanocomposite was confined to the facing layer by surface spraying, powder dusting, suspension incorporation, or a combined route, and to characterize the selected incorporated formulation relative to an unmodified control. The working hypothesis was that suspension incorporation would produce a macroscopically uniform and physically retained silver-bearing phase while preserving the dominant cementitious microstructure and vibrational fingerprint.

2. Materials and methods

2.1. Experimental design

Two-layer paving-block specimens were manufactured with a common structural base and a thinner facing layer designed as the exposed wearing surface. The AgNP modifier was confined exclusively to the facing layer, while the base-layer composition remained constant. Five experimental groups were prepared: CTRL, AgNP-S, AgNP-PD, AgNP-SI, and AgNP-SI+PD (Table 2). Following macroscopic comparison of the fabricated specimens, CTRL and AgNP-SI were selected for detailed SEM-EDS, FTIR, and Raman analyses.

All modified formulations retained the same nominal mineral composition of the facing layer. Consequently, differences in surface appearance and instrumental response were interpreted primarily in relation to the AgNP application route and the presence of the biogenic silver-bearing phase.

2.2. Biogenic silver nanocomposite and cementitious constituents

The silver-containing modifier was the biogenic nanocomposite synthesized using *Lactobacillus paracasei* isolated from whey and previously characterized for physicochemical, antiradical, and antimicrobial

properties [17]. The material contained metallic silver cores with an average size of approximately 18 ± 2.4 nm associated with an organic biomolecular coating [17]. The abbreviation AgNP is retained throughout the manuscript for continuity, although the modifier is more precisely described as an organically capped biogenic silver nanocomposite.

The structural base mixture contained cement, two sand fractions designated Sand L and Sand M, stone dust, and water. The facing mixture contained cement, a size-controlled sand fraction, and water. The nominal mass fractions are summarized in Table 1. No AgNP material was added to the structural base layer.

2.3. Mixture design and specimen fabrication

The nominal base-layer formulation comprised 13.9 mass% cement, 13.9 mass% Sand L, 35.6 mass% Sand M, 31.7 mass% stone dust, and 4.9 mass% water. The nominal facing-layer formulation comprised 15.0 mass% cement, 76.0 mass% size-controlled sand, and 9.0 mass% water. The production sheet specified w/c values of 0.40 for the base layer and 0.62 for the facing layer, while ratios calculated from the rounded mass fractions were 0.35 and 0.60, respectively. Both sets of values are reported to preserve the original formulation record.

The base and facing mixtures were prepared separately. The base mixture was formed as the supporting body, after which the facing mixture was placed as the exposed layer before hardening. Depending on the experimental group, the AgNP modifier was introduced into the facing mixture, applied to the facing surface, or used in both positions.

2.4. AgNP application strategies

Four AgNP application routes were implemented (Table 2). For AgNP-S, an aqueous AgNP suspension at 6.67 mg mL^{-1} was applied to the facing surface by spraying. For AgNP-PD, dry AgNP powder was distributed directly over the facing surface. For AgNP-SI, the AgNP suspension was incorporated into the facing mixture at 0.41 wt% relative to the facing-layer cement mass. AgNP-SI+PD combined suspension incorporation at 0.41 wt% with subsequent surface powder dusting. This design enabled direct comparison of surface deposition, incorporation within the facing layer, and a combined application strategy.

2.5. Selection of the formulation for detailed characterization

After fabrication, the specimens were compared macroscopically with respect to surface uniformity, visible clustering, and continuity of modifier distribution. AgNP-SI showed the most homogeneous modified surface and contained a defined incorporated dose; it was therefore selected for detailed physicochemical comparison with CTRL.

2.6. Scanning electron microscopy and EDS microanalysis

Facing-layer fragments from CTRL and AgNP-SI were examined using a LEO 1430 VP scanning electron microscope (LEO Electron Microscopy Ltd., England) equipped for secondary-electron imaging and variable-pressure operation. Elemental microanalysis and mapping were performed with a Quantax 200 energy-dispersive X-ray system fitted with an XFlash 4010 detector (Bruker AXS, Germany). SEM images were recorded at magnifications ranging from 200× to 200,000×.

The analyzed micrographs documented accelerating voltages of 20–30 kV and working distances of approximately 9.5–10.2 mm. Images were acquired under variable-pressure conditions of 50 Pa or under high vacuum, depending on the field. Comparative EDS spectra and elemental maps were obtained at 700×, 28 kV,

and a working distance of 25 mm. EDS values were interpreted as local semiquantitative microanalysis of the selected interaction volumes.

2.7. Fourier-transform infrared spectroscopy

FTIR spectra of CTRL and AgNP-SI were acquired using a vacuum Vertex 70V spectrometer coupled to a Hyperion 1000 infrared microscope (Bruker Optik, Germany). The comparative spectra covered approximately 3800–400 cm^{-1} and were evaluated as transmittance versus wavenumber. Band assignments were interpreted in relation to established spectral characteristics of hydrated Portland-cement systems [38]–[40].

2.8. Raman spectroscopy

Raman spectra were acquired using a Senterra confocal dispersive Raman spectrometer (Bruker Optik, Germany) equipped with a thermoelectrically cooled CCD detector, video imaging, and a motorized xyz stage. The spectra were evaluated over approximately 1800–100 cm^{-1}. Interpretation focused on the mineral-lattice region and on the AgNP-associated features near 1350 and 1590–1600 cm^{-1}, with reference to the established D- and G-band regions of carbonaceous materials [34] and the principles of Ag-associated Raman enhancement [41].

2.9. Data analysis

Macroscopic appearance, SEM morphology, EDS spectra and maps, and vibrational spectra were compared descriptively. The EDS results were retained in the software-reported units: atomic percent for CTRL and mass percent for AgNP-SI. Because EDS probes selected microvolumes, the values were interpreted as local semiquantitative measurements and were not converted into bulk composition. Approximate FTIR and Raman band positions were read from the comparative spectra.

Table 1. Nominal composition of the structural base and exposed facing layers.

Component or parameter	Base layer	Facing layer
Cement, mass%	13.9	15.0
Sand L, mass%	13.9	—
Sand M, mass%	35.6	—
Size-controlled sand, mass%	—	76.0
Stone dust, mass%	31.7	—
Water, mass%	4.9	9.0
w/c, production-sheet value	0.40	0.62
w/c, calculated from rounded composition	0.35	0.60

Note: all modified specimens used the same nominal mineral formulation in the facing layer. Both production-sheet and composition-derived w/c values are shown because the formulation entries were reported as rounded mass percentages.

Table 2. Experimental groups and AgNP application routes.

Code	Description	Modification strategy
CTRL	Unmodified control	No AgNP addition.
AgNP-S	Surface-sprayed specimen	A 6.67 mg mL^{-1} aqueous AgNP suspension was applied to the facing surface by spraying.

Code	Description	Modification strategy
AgNP-PD	Powder-dusted specimen	Dry AgNP powder was applied directly to the facing surface.
AgNP-SI	Solution-incorporated specimen	AgNP suspension was incorporated into the facing mixture at 0.41 wt% relative to cement.
AgNP-SI+PD	Combined specimen	AgNP suspension was incorporated at 0.41 wt% relative to cement, followed by surface powder dusting.

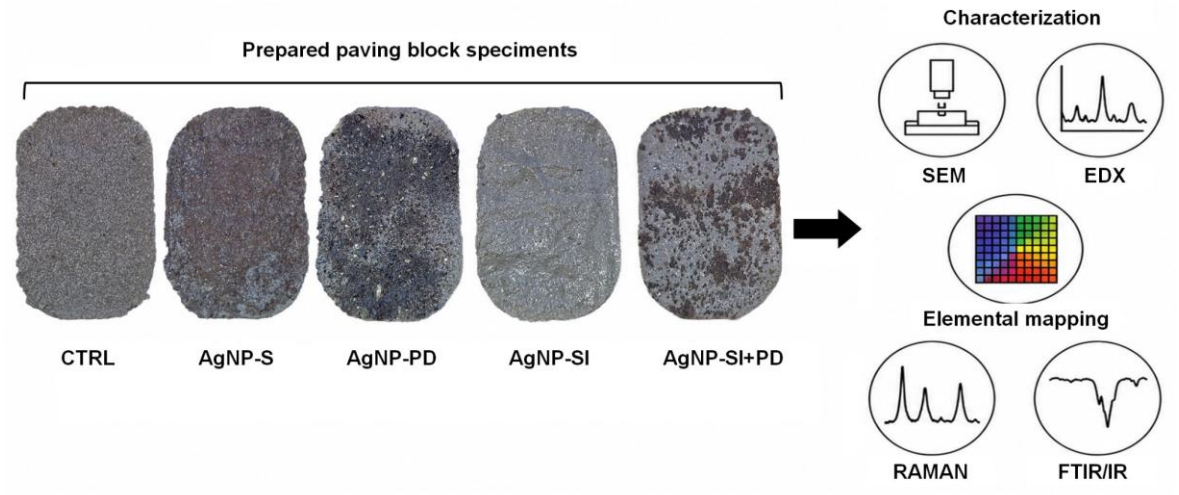

Figure 1. Fabricated two-layer paving-block specimens and analytical workflow. CTRL, unmodified control; AgNP-S, surface spraying; AgNP-PD, surface powder dusting; AgNP-SI, AgNP suspension incorporated into the facing mixture; AgNP-SI+PD, suspension incorporation followed by powder dusting. The detailed physicochemical comparison was performed between CTRL and AgNP-SI using SEM, EDS microanalysis and elemental mapping, FTIR, and Raman spectroscopy.

3. Results

3.1. Macroscopic appearance and selection of AgNP-SI

The five formulations displayed distinct macroscopic surface characteristics after fabrication (Figure 1). CTRL exhibited a comparatively uniform gray facing layer. AgNP-S showed a darker brown-gray surface consistent with a deposited surface film. AgNP-PD had a granular appearance with discrete dark speckles, whereas AgNP-SI retained a relatively uniform gray surface with fine, dispersed heterogeneity. AgNP-SI+PD exhibited the strongest mottling and the highest density of dark surface domains. The surface-only routes therefore produced visibly localized deposits, while suspension incorporation generated a more continuous macroscopic appearance.

On this basis, AgNP-SI was selected for detailed comparison with CTRL. Its homogeneous surface appearance and defined incorporated dose provided a consistent material basis for SEM-EDS and vibrational-spectroscopic analyses.

3.2. SEM morphology of CTRL and AgNP-SI

At 200×, both CTRL and AgNP-SI consisted of irregular aggregate particles and cementitious fines separated by interparticle voids (Figure 2). At 1000× and 5000×, CTRL displayed rough particulate deposits and heterogeneous hydration products, whereas selected AgNP-SI particles showed locally smoother and more continuous surface coverage. At 50,000× and 200,000×, both materials exhibited folded, lamellar, and foil-like nanoscale hydration-product morphologies. AgNP-SI additionally contained locally dense nanoscale deposits. Because fine mineral phases, hydration products, and the organic component of the biogenic nanocomposite can generate similar topographic contrast, silver localization was assessed by EDS rather than morphology alone. No gross cracking, matrix collapse, or qualitative loss of cohesion attributable to the 0.41 wt% treatment was observed in the analyzed fields.

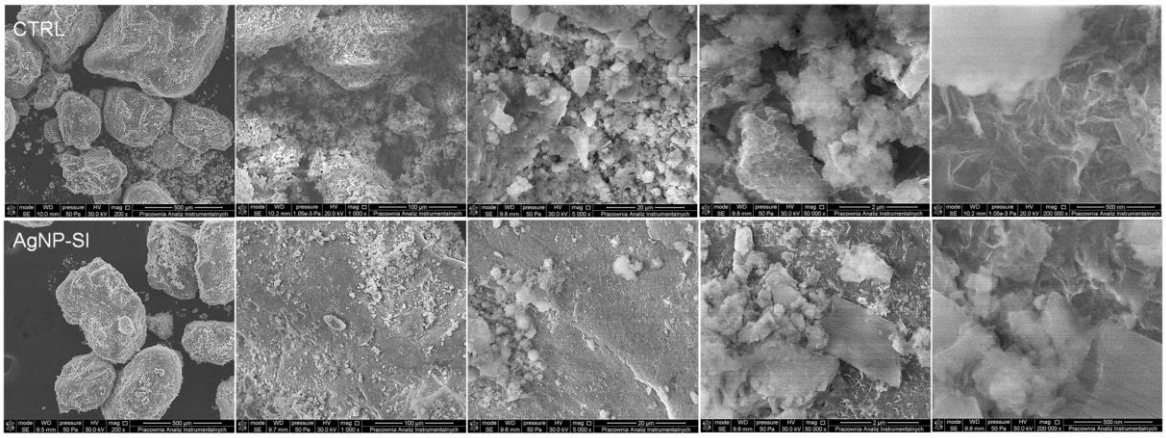

Figure 2. SEM micrographs of CTRL (top row) and AgNP-SI (bottom row) at increasing magnification. Scale bars from left to right: 500 µm, 100 µm, 20 µm, 2 µm, and 500 nm. Both specimens show heterogeneous aggregate and hydration-product morphologies, with locally denser nanoscale surface deposits in AgNP-SI.

3.3. EDS spectra and elemental distribution

The CTRL field was dominated by O, Si, and Ca, with smaller contributions from Al, C, K, S, Fe, Na, Mg, and P, as expected for a silicate-rich cementitious material (Figure 3; Table 3). The software-reported CTRL summary contained 62.28 at% O, 18.11 at% Si, 13.21 at% Ca, 2.39 at% Al, and 1.56 at% C. A minor signal of 0.08 at% Ag was also reported.

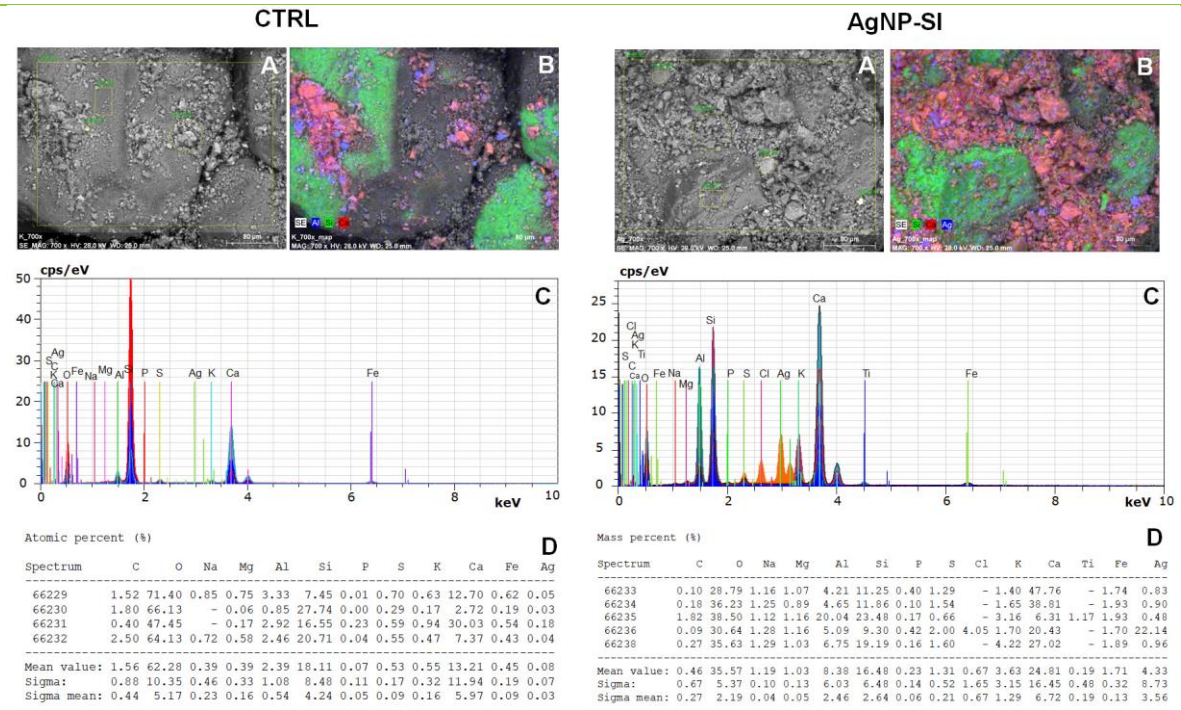

Figure 3. Comparative SEM-EDS analysis of CTRL and AgNP-SI, including representative secondary-electron images, analyzed points and areas, elemental maps, overlaid EDS spectra, and software-reported quantitative summaries. CTRL values are reported in atomic percent and AgNP-SI values in mass percent; the datasets therefore represent separate local semiquantitative summaries.

Because CTRL contained no intentionally added silver and the reported signal was low, the 0.08 at% value was interpreted as a background-level response associated with spectral overlap or incidental analytical contamination rather than a material feature.

The AgNP-SI field contained O, Ca, Si, Al, K, Fe, S, Na, Mg, P, Cl, Ti, C, and Ag. The software-reported mean for the selected modified microareas was 4.33 mass% Ag. Individual point spectra contained 0.83, 0.90, 0.48, 22.14, and 0.96 mass% Ag. Elemental mapping showed silver throughout the analyzed field, with pronounced local intensification. The isolated 22.14 mass% value identified an Ag-rich microdomain, while the remaining points confirmed lower but consistently detectable local silver content.

The 4.33 mass% value represents the selected SEM interaction volumes rather than the bulk Ag concentration of the facing layer. Its magnitude, together with the 0.48–22.14 mass% point range, demonstrates spatial heterogeneity and localized enrichment. Direct numerical comparison with CTRL is not appropriate because the two software exports use different reporting bases.

Table 3. Software-reported local EDS summaries for CTRL and AgNP-SI microareas.

Element	CTRL, atomic%	AgNP-SI, mass%
C	1.56	0.46
O	62.28	35.57
Na	0.39	1.19
Mg	0.39	1.03
Al	2.39	8.38
Si	18.11	16.48
P	0.07	0.23

Element	CTRL, atomic%	AgNP-SI, mass%
S	0.53	1.31
Cl	—	0.67
K	0.55	3.63
Ca	13.21	24.81
Ti	—	0.19
Fe	0.45	1.71
Ag	0.08	4.33

Ag point spectra in AgNP-SI (mass%): 0.83, 0.90, 0.48, 22.14, and 0.96. The values represent local semiquantitative microanalysis; CTRL and AgNP-SI are reported on different numerical bases.

3.4. FTIR characteristics

CTRL and AgNP-SI showed broadly overlapping FTIR profiles (Figure 4A). Both spectra contained a broad high-wavenumber contribution assigned to O-H stretching of adsorbed or bound water and hydroxyl-bearing hydration products, a water-bending region near 1640 cm^{-1}, a carbonate-associated envelope around 1420–1450 cm^{-1}, and a dominant silicate/C-S-H region between approximately 1100 and 950 cm^{-1}. Bands in the 800–780 cm^{-1} region were consistent with quartz or aggregate-related silicate modes, while the strong feature near 460 cm^{-1} was assigned mainly to Si-O deformation or a quartz-related lattice vibration (Table 4).

AgNP-SI differed from CTRL in relative transmittance and band shape, particularly within the silicate and low-wavenumber regions. The principal mineral and hydration-product bands nevertheless remained clearly recognizable, indicating preservation of the dominant cementitious chemical framework after suspension incorporation.

3.5. Raman characteristics

The Raman spectra retained prominent low-wavenumber mineral bands, including a strong feature near 460 cm^{-1} and additional bands around 200 and 130 cm^{-1} (Figure 4B). Relative to CTRL, AgNP-SI exhibited markedly intensified broad features near 1350 and 1590–1600 cm^{-1}, together with a modified background and greater overall signal intensity. These regions correspond to the conventional D- and G-type bands of disordered and graphitic carbonaceous structures [34].

The intensified bands are consistent with carbonaceous or biomolecular components of the organic coating previously characterized in the biogenic AgNP material [17]. Their enhancement may also reflect stronger local Raman scattering in Ag-rich domains, in agreement with established plasmonic enhancement principles [41]. The Raman response therefore represents an AgNP-associated carbonaceous contribution superimposed on the mineral spectrum of the cementitious matrix.

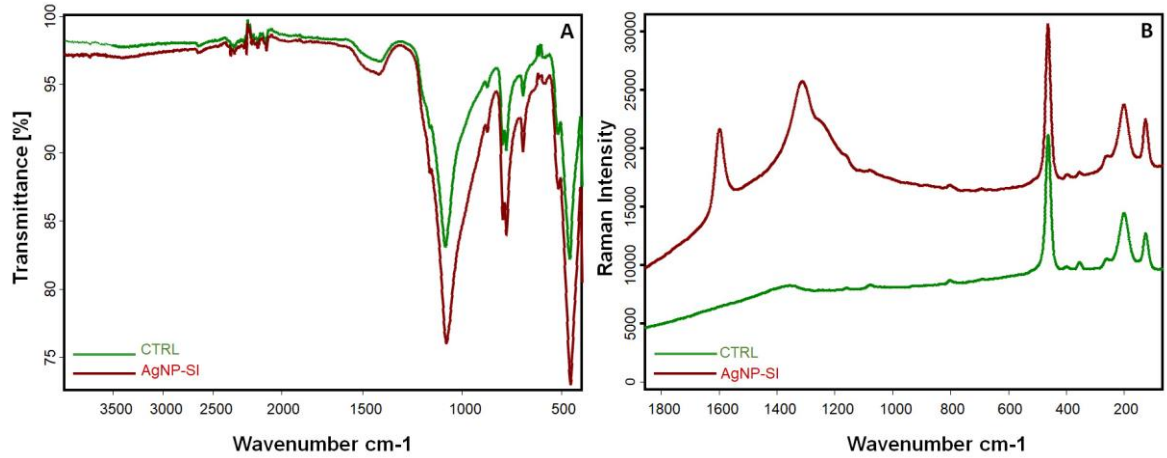

Figure 4. Vibrational-spectroscopy comparison of CTRL and AgNP-SI. (A) FTIR spectra presented as transmittance versus wavenumber. (B) Raman spectra displayed with vertical offset for clarity. Approximate band positions are summarized in Table 4.

Table 4. Assignment and interpretation of the principal FTIR and Raman features.

Technique	Approximate position	Provisional assignment	Interpretive constraint
FTIR	~3400 cm^{-1}	O-H stretching of bound/adsorbed water and hydroxyl-bearing hydration products	Hydrated matrix contribution in both specimens.
FTIR	~1640 cm^{-1}	H-O-H bending of molecular water	Consistent with retained molecular water in the hydrated cementitious matrix.
FTIR	~1420–1450 cm^{-1}	Carbonate stretching	Carbonate-containing phases and carbonation products.
FTIR	~1100–950 cm^{-1}	Si-O stretching in silicate/C-S-H environments; possible sulfate overlap	Dominant cementitious envelope in both specimens.
FTIR	~800–780 cm^{-1}	Quartz or aggregate-related silicate modes	Contribution from the mineral aggregate fraction.
FTIR/Raman	~460 cm^{-1}	Si-O deformation or quartz-related lattice mode	Strong in both materials, supporting preservation of the mineral framework.
Raman	~1350 cm^{-1}	D-type band of disordered carbon and AgNP-associated surface contribution	Enhanced in AgNP-SI and consistent with the organic biogenic coating.
Raman	~1590–1600 cm^{-1}	G-type carbon band with possible local Ag-associated scattering enhancement	Enhanced in AgNP-SI; compatible with carbonaceous coating and Ag-rich microdomains.

4. Discussion

4.1. Significance of the two-layer architecture and application route

The two-layer architecture offers an efficient way to localize a functional phase at the exposed surface while retaining a conventional supporting base [8], [9], [11]. In the present specimens, all AgNP variants shared the same structural layer and facing-layer mineral formulation; therefore, the observed macroscopic differences primarily reflected the mode of modifier introduction. Concentrating AgNPs within the facing layer also limits silver consumption relative to full-volume modification and places the silver-bearing phase close to the interface at which contamination would occur.

AgNP-SI showed a more homogeneous macroscopic surface than the powder-dusted formulations, which contained clearly visible dark speckles and mottled deposits. This observation agrees with Ceran et al. [9], who found that dispersed AgNPs were generally incorporated more favorably than powdered material and that excessive powder addition promoted agglomeration. The incorporated dose used here, 0.41 wt% relative to facing-layer cement, was substantially lower than the 1–5 wt% colloidal AgNP loadings investigated by Nam [33] and the multi-percent additions assessed by Ceran et al. [9]. The low-dose result is also conceptually consistent with the CuO study of Ślosarczyk et al. [54], in which the best compromise between functional and engineering properties occurred at the lowest tested nanoparticle addition, although CuO and Ag differ in chemistry and mode of action.

The four fabrication routes generated distinct spatial states of the modifier. Spraying produced a surface film, powder dusting generated discrete deposits, suspension incorporation distributed the modifier through the facing mixture, and the combined route superimposed internal incorporation with a surface-rich powder fraction. The comparatively continuous appearance of AgNP-SI and the subsequent EDS confirmation of retained silver support suspension incorporation as the most coherent route when uniform facing-layer distribution is prioritized. By contrast, surface treatments such as those reported by Noeiaghaei et al. [8] and Graziani et al. [10] favor immediate surface accessibility but are more strongly governed by substrate roughness, porosity, and coating continuity.

4.2. Microstructure and elemental evidence for retained silver

SEM did not reveal gross deterioration of the hydrated matrix after incorporation of the 0.41 wt% AgNP dose. This finding is compatible with studies showing that controlled silver-nanoparticle additions can be accommodated by cementitious systems without obligatory loss of matrix integrity [9], [30], [33]. The locally smoother and more continuous coverage observed on selected AgNP-SI particles may reflect fine-particle filling, deposition of the biomolecular coating, or a local redistribution of hydration products. Irrespective of the mechanism, the coexistence of conventional lamellar and foil-like hydration morphologies in CTRL and AgNP-SI indicates that the dominant cementitious microstructure was retained.

Secondary-electron morphology alone cannot identify nanosilver reliably within a cement matrix because fine mineral phases, hydration products, carbonaceous residues, and Ag-containing domains can overlap in apparent size and topographic contrast [35]–[37]. EDS therefore provides the direct evidence for silver retention in AgNP-SI. The elemental map and point spectra showed Ag throughout the analyzed field together with localized enrichment, demonstrating that the incorporated biogenic nanocomposite formed a heterogeneous rather than perfectly uniform microdistribution.

The Ag-rich microdomains are consistent with local aggregation of the organically capped nanocomposite or preferential accumulation within pores and hydration-product interfaces. Such heterogeneity is expected because AgNP behavior depends on particle geometry, aggregation state, surface oxidation, and dissolution kinetics [14], [16], [20], [21]. Ceran et al. [9] similarly identified agglomeration as a central limitation of powdered AgNP incorporation. In the present material, the coexistence of low-Ag points and an isolated

22.14 mass% Ag point indicates that most of the analyzed matrix contained dispersed silver-bearing material interspersed with locally concentrated domains.

The software-reported mean of 4.33 mass% Ag must be interpreted at the scale of the selected EDS interaction volumes. It does not represent the bulk composition of the facing layer and is fully compatible with the nominal 0.41 wt% dose relative to cement when the electron beam intersects an Ag-rich microdomain. EDS quantification is sensitive to local topography, interaction volume, matrix composition, and correction procedure [35]–[37]. The trace 0.08 at% Ag signal in CTRL is therefore best understood as analytical background, whereas the spatially coherent Ag map and repeated Ag-positive point spectra in AgNP-SI constitute the relevant evidence of modifier retention.

4.3. Interpretation of FTIR and Raman changes

The broad overlap of CTRL and AgNP-SI FTIR spectra shows that suspension incorporation did not replace the principal silicate, carbonate, and hydration-product signatures. The observed bands agree with established assignments for Portland-cement systems, including O-H-containing hydration products, molecular water, carbonate species, Si-O stretching in silicate and C-S-H environments, quartz-related modes, and low-wavenumber Si-O deformation [38]–[40]. Because the AgNP modifier represented a minor fraction of the mineral matrix, preservation of the dominant FTIR envelope is consistent with the SEM evidence of microstructural continuity.

The absence of an isolated Ag-specific FTIR band is chemically reasonable because metallic silver does not generate a strong, unique molecular vibration in the conventional mid-infrared region, while low-concentration organic surface species are superimposed on intense cement and aggregate absorptions. FTIR is therefore most informative here as evidence that the matrix-level chemical framework remained recognizable. The modest differences in relative transmittance and band shape likely reflect local changes in hydration-product distribution, carbonate content, or the contribution of the biogenic organic coating.

The Raman response provided a more distinctive signature of the incorporated modifier. The broad features near 1350 and 1590–1600 cm^{-1} coincide with the D- and G-band regions of disordered and graphitic carbonaceous structures [34]. Their marked intensification in AgNP-SI is consistent with the biomolecular coating previously identified for the *Lactobacillus*-derived silver nanocomposite [17]. Incorporation into the alkaline cementitious matrix and interaction with mineral surfaces may alter the organization and optical response of these carbonaceous components, making them more prominent relative to CTRL.

A local Ag-associated enhancement of Raman scattering is also plausible because electromagnetic amplification can occur near plasmonic silver nanostructures, especially at rough surfaces and junctions between Ag-rich domains [41]. The Ag hotspots detected by EDS provide a physically coherent basis for this contribution. The most balanced interpretation is therefore that the intensified Raman bands arise from the carbonaceous biogenic coating, potentially amplified locally by the silver-containing microstructure, rather than from a new bulk cement phase.

4.4. Comparison with antimicrobial cementitious systems and veterinary relevance

The functional rationale for incorporating AgNPs into a livestock-facility surface is supported by the extensive literature on particle- and ion-mediated antimicrobial activity [12]–[29]. However, immobilization within hydrated cement changes the chemical environment governing that activity. High alkalinity, chloride, sulfide, phosphate, carbonate, and organic ligands can alter Ag oxidation, dissolution, aggregation, and speciation [18]–[21], [25], [26]. The EDS-confirmed silver-bearing domains observed here establish the required

material-level presence of the modifier, while their heterogeneous distribution is likely to influence the balance between surface accessibility, ionic release, and retention.

Direct comparison with published antimicrobial cement systems highlights the importance of dose and exposure conditions. Nam [33] incorporated 1, 3, and 5 wt% colloidal AgNPs into Portland cement and reported dose-dependent silver release, shorter setting time at higher loading, preserved compressive strength, and antibacterial inhibition at 5 wt%. Noeiaghaei et al. [8] reported more than 60% reduction of *Bacillus cereus* and *Escherichia coli* during a seven-day surface-treatment experiment using 250 mg L^{-1} nanoparticle suspensions. Vázquez-García et al. [30] likewise demonstrated that AgNPs can modify the physicochemical and antibacterial properties of calcium-silicate cements. The present 0.41 wt% biogenic formulation therefore occupies a distinctly lower-dose and structurally localized design space than these incorporated or surface-treated systems.

Hybrid and alternative nanoparticle systems further illustrate the need to balance functional activity with matrix performance. Ünal et al. [31] achieved sustained antibacterial behavior using Ag-modified TiO_2 in mortar and concrete, while Sybis et al. [32] examined nanosilver-modified concrete in the context of structural resilience. In CuO-doped engineered cementitious composites, Ślosarczyk et al. [54] found that the lowest tested dose provided the most favorable overall compromise between antibacterial, mechanical, structural, and durability properties. Together with the dispersed-versus-powdered comparison of Ceran et al. [9], these studies support the present emphasis on route-controlled localization and low-dose incorporation rather than nominal silver content alone (Table 5).

The veterinary relevance of silver also extends to viruses of major animal and public-health importance. Antiviral effects of AgNP-based systems have been reported against African swine fever virus [42], influenza A/H1N1 [43]–[45], avian influenza H9N2 and H5N1 [46], [47], HIV-1 [48], [49], monkeypox virus [50], SARS-CoV-2 [51], Rift Valley fever virus [52], and porcine reproductive and respiratory syndrome virus [53]. These studies demonstrate broad, virus-dependent biological plausibility across dispersed nanoparticles and composite systems. They also show that particle chemistry, formulation, virus type, and exposure conditions strongly determine the outcome; consequently, they provide a mechanistic and veterinary context for the present material rather than a direct performance benchmark for a cementitious paving surface.

Table 5. Comparison of the present material concept with representative antimicrobial cementitious systems.

Study	Material and route	Principal reported outcome	Relevance to the present work
Present study	Biogenic AgNP suspension incorporated into the facing layer at 0.41 wt% relative to cement; surface spraying, powder dusting, and a combined route also fabricated.	Route-dependent surface appearance; retained Ag and Ag-rich microdomains confirmed by SEM-EDS; dominant cementitious FTIR profile preserved.	Demonstrates selective facing-layer functionalization at a comparatively low incorporated dose.
Nam [33]	Colloidal AgNPs incorporated into Portland cement at 1, 3, and 5 wt%.	Dose-dependent Ag release; higher loading shortened setting; antibacterial inhibition reported at 5 wt%; compressive strength remained comparable.	Provides a higher-dose incorporated AgNP comparator and demonstrates dose-sensitive material and antibacterial responses.
Noeiaghaei et al. [8]	Surface treatment with Ag or ZnO nanoparticle suspensions; 250 mg L^{-1} in the reported bactericidal experiments.	>60% viable-cell reduction after seven days under the tested pH conditions when treatment was applied at the start of culture.	Illustrates the high accessibility of a surface-applied modifier under prolonged aqueous contact.

Study	Material and route	Principal reported outcome	Relevance to the present work
Ceran et al. [9]	Dispersed and powdered AgNP additions to cementitious composites.	Dispersed AgNPs generally produced more favorable composite behavior; powdered AgNPs were increasingly limited by agglomeration.	Consistent with the more uniform appearance of suspension incorporation than powder dusting in the present study.
Ślosarczyk et al. [54]	CuO nanoparticles incorporated at 0.25, 0.50, and 1.00 wt%.	All doses improved antibacterial properties; 0.25 wt% provided the best overall balance of mechanical, structural, and durability characteristics.	Shows that a low nanoparticle dose can optimize combined functional and engineering properties, although CuO chemistry differs from Ag.
Ünal et al. [31]	Mechanically alloyed Ag-modified TiO_2 incorporated into mortar and concrete.	Sustained antibacterial activity under controlled repeated-challenge conditions.	Demonstrates durable antibacterial function in a hybrid photocatalytic/Ag system.

4.5. Engineering, release, and regulatory context

Concrete paving blocks are engineering products whose dimensions, strength, water absorption, abrasion resistance, and freeze-thaw behavior are addressed within the EN 1338 framework [55]. At the microstructural level, the present SEM and FTIR results indicate that the 0.41 wt% AgNP incorporation preserved the recognizable hydrated cementitious framework. This observation is consistent with reports that nanoparticle-modified cement systems can retain acceptable structural characteristics when dose and dispersion are controlled [9], [30], [33], [54].

Selective placement of the Ag-bearing phase in the facing layer is also relevant to environmental behavior because this layer forms the direct interface with water, cleaning agents, and mechanical wear. Studies of nanosilver-containing textiles and outdoor facades have demonstrated that silver can migrate from functional materials into water and runoff [56], [57]. The retained Ag distribution observed by EDS in AgNP-SI therefore defines the initial material state from which any subsequent transport or transformation would originate.

Released silver may occur as dissolved ions, nanoparticles, aggregates, or transformed species, with oxidation, sulfidation, chlorination, and complexation governing persistence and biological availability [58]. These transformations are central to the molecular toxicity of nanosilver [59] and to comparative environmental hazard across Ag, CuO, and ZnO nanomaterials [60]. In a cementitious matrix, the observed localization of Ag within microdomains is therefore relevant not only to functional accessibility but also to retention and speciation.

ISO 22196 and ISO 21702 provide standardized terminology and measurement principles for antibacterial and antiviral activity on non-porous surfaces [61], [62]. A rough and absorbent cementitious surface differs substantially from the substrates for which those methods were designed, particularly in inoculum recovery, moisture retention, and contact geometry. In parallel, Regulation (EU) No 528/2012 governs the placing on the market and use of biocidal products and treated articles [63]. For this reason, the present material is described strictly in physicochemical terms as AgNP-modified rather than assigned an antibacterial, antiviral, or biocidal performance claim.

The literature on acquired silver tolerance [22], [23] further supports a restrained application concept in which a silver-modified surface complements, rather than replaces, cleaning, disinfection, controlled access, and footwear management. This positioning is consistent with the layered biosecurity principles established for pig and poultry production [1]–[7].

5. Conclusions

Two-layer concrete paving blocks were successfully fabricated using four AgNP application routes confined to the facing layer. Suspension incorporation at 0.41 wt% relative to facing-layer cement produced the most macroscopically homogeneous modified specimen and enabled a controlled comparison with the unmodified material. SEM showed preservation of the characteristic heterogeneous cementitious microstructure, while EDS spectra and elemental mapping confirmed retained silver and revealed a distribution composed of dispersed Ag-bearing regions and localized Ag-rich microdomains. FTIR demonstrated continuity of the dominant silicate, carbonate, and hydration-product framework. Raman spectroscopy identified intensified bands near 1350 and 1590–1600 cm^{-1}, consistent with the carbonaceous biomolecular coating of the biogenic nanocomposite and a possible local Ag-associated enhancement of scattering. Collectively, these results establish a coherent physicochemical basis for selectively functionalizing the wearing layer of concrete paving units with a biogenic silver nanocomposite while preserving the recognizable cementitious matrix.

Acknowledgments

The authors gratefully acknowledge that the scientific collaboration underlying this study was initiated during implementation of the project “BioCoLL: Tailor-Made Biocolloids—Intelligent Systems of Microorganisms and Metal–Protein Nanocomposites for the Economy of Tomorrow.” The project is implemented under the Foundation for Polish Science PRIME programme, grant no. PRIME 2.06-0135/25 FENG, from 1 June 2025 to 30 November 2026. The project environment facilitated the interdisciplinary cooperation and exchange of scientific expertise that contributed to the development of the present study.

Ethics approval and consent to participate

Not applicable. The study did not involve humans or live animals.

Consent for publication

Not applicable.

Data availability

The representative images, comparative spectra, and EDS summaries supporting the findings of this study are included in the article.

References

[1] L. V. Alarcón, A. Allepuz, i E. Mateu, „Biosecurity in pig farms: a review”, *Porc Health Manag*, t. 7, nr 1, s. 5, sty. 2021, doi: 10.1186/s40813-020-00181-z.

[2] N. A. Rimi *et al.*, „Biosecurity Conditions in Small Commercial Chicken Farms, Bangladesh 2011–2012”, *EcoHealth*, t. 14, nr 2, s. 244–258, cze. 2017, doi: 10.1007/s10393-017-1224-2.

[3] O. L. Harrison *et al.*, „Evaluating dry vs. wet disinfection in boot baths on detection of porcine epidemic diarrhea virus and porcine reproductive and respiratory virus RNA”, *Translational Animal Science*, t. 6, nr 4, s. txac150, paź. 2022, doi: 10.1093/tas/txac150.

[4] G. De Lorenzi, L. Borella, G. L. Alborali, J. Prodanov-Radulović, M. Štukelj, i S. Bellini, „African swine fever: A review of cleaning and disinfection procedures in commercial pig holdings”, *Research in Veterinary Science*, t. 132, s. 262–267, paź. 2020, doi: 10.1016/j.rvsc.2020.06.009.

[5] M. S. Beato, F. D’Errico, C. Iscaro, S. Petrini, M. Giammarioli, i F. Feliziani, „Disinfectants against African Swine Fever: An Updated Review”, *Viruses*, t. 14, nr 7, s. 1384, cze. 2022, doi: 10.3390/v14071384.

[6] S. A. E. Nasr *et al.*, „Effectiveness of Some Disinfectants Commonly Used in footbaths inside Poultry Farms”.

[7] S. Otake *et al.*, „Transmission of porcine reproductive and respiratory syndrome virus by fomites (boots and coveralls)”, *JSHAP*, t. 10, nr 2, s. 59–65, mar. 2002, doi: 10.54846/jshap/329.

[8] T. Noeiaghaei, N. Dhami, i A. Mukherjee, „Nanoparticles surface treatment on cemented materials for inhibition of bacterial growth”, *Construction and Building Materials*, t. 150, s. 880–891, wrz. 2017, doi: 10.1016/j.conbuildmat.2017.06.046.

[9] Ö. B. Ceran, B. Şimşek, S. Doruk, T. Uygunoğlu, i O. N. Şara, „Effects of dispersed and powdered silver nanoparticles on the mechanical, thermal, electrical and durability properties of cementitious composites”, *Construction and Building Materials*, t. 222, s. 152–167, paź. 2019, doi: 10.1016/j.conbuildmat.2019.06.138.

[10] L. Graziani, E. Quagliarini, i M. D’Orazio, „The role of roughness and porosity on the self-cleaning and anti-biofouling efficiency of TiO2-Cu and TiO2-Ag nanocoatings applied on fired bricks”, *Construction and Building Materials*, t. 129, s. 116–124, grud. 2016, doi: 10.1016/j.conbuildmat.2016.10.111.

[11] L. Qiu, S. Dong, A. Ashour, i B. Han, „Antimicrobial concrete for smart and durable infrastructures: A review”, *Construction and Building Materials*, t. 260, s. 120456, lis. 2020, doi: 10.1016/j.conbuildmat.2020.120456.

[12] I. Sondi i B. Salopek-Sondi, „Silver nanoparticles as antimicrobial agent: a case study on E. coli as a model for Gram-negative bacteria”, *Journal of Colloid and Interface Science*, t. 275, nr 1, s. 177–182, lip. 2004, doi: 10.1016/j.jcis.2004.02.012.

[13] J. R. Morones *et al.*, „The bactericidal effect of silver nanoparticles”, *Nanotechnology*, t. 16, nr 10, s. 2346–2353, paź. 2005, doi: 10.1088/0957-4484/16/10/059.

[14] S. Pal, Y. K. Tak, i J. M. Song, „Does the Antibacterial Activity of Silver Nanoparticles Depend on the Shape of the Nanoparticle? A Study of the Gram-Negative Bacterium *Escherichia coli*”, *Appl Environ Microbiol*, t. 73, nr 6, s. 1712–1720, mar. 2007, doi: 10.1128/AEM.02218-06.

[15] J. S. Kim *et al.*, „Antimicrobial effects of silver nanoparticles”, *Nanomedicine: Nanotechnology, Biology and Medicine*, t. 3, nr 1, s. 95–101, mar. 2007, doi: 10.1016/j.nano.2006.12.001.

[16] C.-N. Lok *et al.*, „Silver nanoparticles: partial oxidation and antibacterial activities”, *J Biol Inorg Chem*, t. 12, nr 4, s. 527–534, maja 2007, doi: 10.1007/s00775-007-0208-z.

[17] R.-P. Viorica, P. Pawel, i B. Boguslaw, „Use of Lactobacillus paracasei isolated from whey for silver nanocomposite synthesis: Antiradical and antimicrobial properties against selected pathogens”, *Journal of Dairy Science*, t. 104, nr 3, s. 2480–2498, mar. 2021, doi: 10.3168/jds.2020-19049.

[18] O. Choi, K. K. Deng, N.-J. Kim, L. Ross, R. Y. Surampalli, i Z. Hu, „The inhibitory effects of silver nanoparticles, silver ions, and silver chloride colloids on microbial growth”, *Water Research*, t. 42, nr 12, s. 3066–3074, cze. 2008, doi: 10.1016/j.watres.2008.02.021.

[19] Z. Xiu, Q. Zhang, H. L. Puppala, V. L. Colvin, i P. J. J. Alvarez, „Negligible Particle-Specific Antibacterial Activity of Silver Nanoparticles”, *Nano Lett.*, t. 12, nr 8, s. 4271–4275, sie. 2012, doi: 10.1021/nl301934w.

[20] S. Kittler, C. Greulich, J. Diendorf, M. Köller, i M. Epple, „Toxicity of Silver Nanoparticles Increases during Storage Because of Slow Dissolution under Release of Silver Ions”, *Chem. Mater.*, t. 22, nr 16, s. 4548–4554, sie. 2010, doi: 10.1021/cm100023p.

[21] J. Liu i R. H. Hurt, „Ion Release Kinetics and Particle Persistence in Aqueous Nano-Silver Colloids”, *Environ. Sci. Technol.*, t. 44, nr 6, s. 2169–2175, mar. 2010, doi: 10.1021/es9035557.

[22] A. Panáček *et al.*, „Bacterial resistance to silver nanoparticles and how to overcome it”, *Nature Nanotech*, t. 13, nr 1, s. 65–71, sty. 2018, doi: 10.1038/s41565-017-0013-y.

[23] J. L. Graves *et al.*, „Rapid evolution of silver nanoparticle resistance in Escherichia coli", *Front. Genet.*, t. 6, lut. 2015, doi: 10.3389/fgene.2015.00042.

[24] T. C. Dakal, A. Kumar, R. S. Majumdar, i V. Yadav, „Mechanistic Basis of Antimicrobial Actions of Silver Nanoparticles", *Front. Microbiol.*, t. 7, lis. 2016, doi: 10.3389/fmicb.2016.01831.

[25] J.-Y. Maillard i P. Hartemann, „Silver as an antimicrobial: facts and gaps in knowledge", *Critical Reviews in Microbiology*, t. 39, nr 4, s. 373–383, lis. 2013, doi: 10.3109/1040841X.2012.713323.

[26] K. Niska, N. Knap, A. Kędzia, M. Jaskiewicz, W. Kamysz, i I. Inkielewicz-Stepniak, „Capping Agent-Dependent Toxicity and Antimicrobial Activity of Silver Nanoparticles: An *In Vitro* Study. Concerns about Potential Application in Dental Practice", *Int. J. Med. Sci.*, t. 13, nr 10, s. 772–782, 2016, doi: 10.7150/ijms.16011.

[27] G. Franci *et al.*, „Silver Nanoparticles as Potential Antibacterial Agents", *Molecules*, t. 20, nr 5, s. 8856–8874, maja 2015, doi: 10.3390/molecules20058856.

[28] M. Rai, A. Yadav, i A. Gade, „Silver nanoparticles as a new generation of antimicrobials", *Biotechnology Advances*, t. 27, nr 1, s. 76–83, sty. 2009, doi: 10.1016/j.biotechadv.2008.09.002.

[29] S. P. Deshmukh, S. M. Patil, S. B. Mullani, i S. D. Delekar, „Silver nanoparticles as an effective disinfectant: A review", *Materials Science and Engineering: C*, t. 97, s. 954–965, kwi. 2019, doi: 10.1016/j.msec.2018.12.102.

[30] F. Vazquez-Garcia *et al.*, „Effect of Silver Nanoparticles on Physicochemical and Antibacterial Properties of Calcium Silicate Cements", *Braz. Dent. J.*, t. 27, nr 5, s. 508–514, paź. 2016, doi: 10.1590/0103-6440201600689.

[31] S. Ünal, M. Orhan, i M. Canbaz, „Sustainable antibacterial performance in cementitious systems using Ag-modified TiO2 compounds", *Front. Struct. Civ. Eng.*, t. 19, nr 7, s. 1061–1074, lip. 2025, doi: 10.1007/s11709-025-1187-2.

[32] M. Sybis, J. Staninska-Pięta, A. Piotrowska-Cyplik, i E. Konował, „Nanosilver Modified Concrete as a Sustainable Strategy for Enhancing Structural Resilience to Flooding", *Sustainability*, t. 18, nr 2, s. 945, sty. 2026, doi: 10.3390/su18020945.

[33] K. Y. Nam, „Characterization and antimicrobial efficacy of Portland cement impregnated with silver nanoparticles", *J Adv Prosthodont*, t. 9, nr 3, s. 217, 2017, doi: 10.4047/jap.2017.9.3.217.

[34] A. C. Ferrari i J. Robertson, „Interpretation of Raman spectra of disordered and amorphous carbon", *Phys. Rev. B*, t. 61, nr 20, s. 14095–14107, maja 2000, doi: 10.1103/PhysRevB.61.14095.

[35] K. L. Scrivener, „Backscattered electron imaging of cementitious microstructures: understanding and quantification", *Cement and Concrete Composites*, t. 26, nr 8, s. 935–945, lis. 2004, doi: 10.1016/j.cemconcomp.2004.02.029.

[36] P. Stutzman, „Scanning electron microscopy imaging of hydraulic cement microstructure", *Cement and Concrete Composites*, t. 26, nr 8, s. 957–966, lis. 2004, doi: 10.1016/j.cemconcomp.2004.02.043.

[37] J. E. Rossen i K. L. Scrivener, „Optimization of SEM-EDS to determine the C–A–S–H composition in matured cement paste samples", *Materials Characterization*, t. 123, s. 294–306, sty. 2017, doi: 10.1016/j.matchar.2016.11.041.

[38] R. Ylmén, U. Jäglid, B.-M. Steenari, i I. Panas, „Early hydration and setting of Portland cement monitored by IR, SEM and Vicat techniques", *Cement and Concrete Research*, t. 39, nr 5, s. 433–439, maja 2009, doi: 10.1016/j.cemconres.2009.01.017.

[39] M. Horgnies, J. J. Chen, i C. Bouillon, „Overview about the use of Fourier Transform Infrared spectroscopy to study cementitious materials", zaprezentowano na MATERIALS CHARACTERISATION 2013, Siena, Italy, cze. 2013, s. 251–262. doi: 10.2495/MC130221.

[40] I. G. Richardson, „The calcium silicate hydrates", *Cement and Concrete Research*, t. 38, nr 2, s. 137–158, lut. 2008, doi: 10.1016/j.cemconres.2007.11.005.

[41] M. Moskovits, „Surface-enhanced spectroscopy", *Rev. Mod. Phys.*, t. 57, nr 3, s. 783–826, lip. 1985, doi: 10.1103/RevModPhys.57.783.

[42] T. Thi Ngoc Dung *et al.*, „Silver nanoparticles as potential antiviral agents against African swine fever virus", *Mater. Res. Express*, t. 6, nr 12, s. 1250g9, sty. 2020, doi: 10.1088/2053-1591/ab6ad8.

[43] D. Xiang, Q. Chen, L. Pang, i C. Zheng, „Inhibitory effects of silver nanoparticles on H1N1 influenza A virus in vitro", *Journal of Virological Methods*, t. 178, nr 1–2, s. 137–142, grud. 2011, doi: 10.1016/j.jviromet.2011.09.003.

[44] Y. Mori, T. Ono, Y. Miyahira, V. Q. Nguyen, T. Matsui, i M. Ishihara, „Antiviral activity of silver nanoparticle/chitosan composites against H1N1 influenza A virus", *Nanoscale Res Lett*, t. 8, nr 1, s. 93, grud. 2013, doi: 10.1186/1556-276X-8-93.

[45] K. Naumenko, S. Zahorodnia, C. V. Pop, i N. Rizun, „Antiviral activity of silver nanoparticles against the influenza A virus", *Journal of Virus Eradication*, t. 9, nr 2, s. 100330, cze. 2023, doi: 10.1016/j.jve.2023.100330.

[46] M. J. Saadh, M. M. Aggag, A. Alboghdadly, A. M. Kharshid, S. M. Aldalaen, i M. A. Abdelrazek, „Silver nanoparticles with epigallocatechingallate and zinc sulphate significantly inhibits avian influenza A virus H9N2", *Microbial Pathogenesis*, t. 158, s. 105071, wrz. 2021, doi: 10.1016/j.micpath.2021.105071.

[47] M. J. Saadh i S. M. Aldalaen, „Inhibitory effects of epigallocatechin gallate (EGCG) combined with zinc sulfate and silver nanoparticles on avian influenza A virus subtype H5N1", *European Review for Medical and Pharmacological Sciences*, t. 25, nr 6, s. 2630–2636, mar. 2021, doi: 10.26355/eurrev_202103_25427.

[48] J. L. Elechiguerra *et al.*, „Interaction of silver nanoparticles with HIV-1", *J Nanobiotechnol*, t. 3, nr 1, s. 6, cze. 2005, doi: 10.1186/1477-3155-3-6.

[49] H. H. Lara, N. V. Ayala-Nuñez, L. Ixtepan-Turrent, i C. Rodriguez-Padilla, „Mode of antiviral action of silver nanoparticles against HIV-1", *J Nanobiotechnol*, t. 8, nr 1, s. 1, 2010, doi: 10.1186/1477-3155-8-1.

[50] J. V. Rogers, C. V. Parkinson, Y. W. Choi, J. L. Speshock, i S. M. Hussain, „A Preliminary Assessment of Silver Nanoparticle Inhibition of Monkeypox Virus Plaque Formation", *Nanoscale Res Lett*, t. 3, nr 4, s. 129–133, kwi. 2008, doi: 10.1007/s11671-008-9128-2.

[51] S. S. Jeremiah, K. Miyakawa, T. Morita, Y. Yamaoka, i A. Ryo, „Potent antiviral effect of silver nanoparticles on SARS-CoV-2", *Biochemical and Biophysical Research Communications*, t. 533, nr 1, s. 195–200, lis. 2020, doi: 10.1016/j.bbrc.2020.09.018.

[52] B. Borrego *et al.*, „Potential application of silver nanoparticles to control the infectivity of Rift Valley fever virus in vitro and in vivo", *Nanomedicine: Nanotechnology, Biology and Medicine*, t. 12, nr 5, s. 1185–1192, lip. 2016, doi: 10.1016/j.nano.2016.01.021.

[53] S. P. Graham *et al.*, „Antiviral Efficacy of Metal and Metal Oxide Nanoparticles against the Porcine Reproductive and Respiratory Syndrome Virus", *Nanomaterials*, t. 11, nr 8, s. 2120, sie. 2021, doi: 10.3390/nano11082120.

[54] A. Ślosarczyk *et al.*, „Antimicrobial action and chemical and physical properties of CuO-doped engineered cementitious composites", *Sci Rep*, t. 13, nr 1, s. 10404, cze. 2023, doi: 10.1038/s41598-023-37673-1.

[55] EN 1338:2003 European Committee for Standardization, „Concrete paving blocks—requirements and test methods", European Committee for Standardization, Brussels, EN 1338:2003 + AC:2006 EN 1338:2003 + AC:2006, 2006.

[56] T. M. Benn i P. Westerhoff, „Nanoparticle Silver Released into Water from Commercially Available Sock Fabrics", *Environ. Sci. Technol.*, t. 42, nr 11, s. 4133–4139, cze. 2008, doi: 10.1021/es7032718.

[57] R. Kaegi *et al.*, „Release of silver nanoparticles from outdoor facades", *Environmental Pollution*, t. 158, nr 9, s. 2900–2905, wrz. 2010, doi: 10.1016/j.envpol.2010.06.009.

[58] B. Reidy, A. Haase, A. Luch, K. Dawson, i I. Lynch, „Mechanisms of Silver Nanoparticle Release, Transformation and Toxicity: A Critical Review of Current Knowledge and Recommendations for Future Studies and Applications", *Materials*, t. 6, nr 6, s. 2295–2350, cze. 2013, doi: 10.3390/ma6062295.

[59] D. McShan, P. C. Ray, i H. Yu, „Molecular toxicity mechanism of nanosilver", *Journal of Food and Drug Analysis*, t. 22, nr 1, s. 116–127, mar. 2014, doi: 10.1016/j.jfda.2014.01.010.

[60] O. Bondarenko, K. Juganson, A. Ivask, K. Kasemets, M. Mortimer, i A. Kahru, „Toxicity of Ag, CuO and ZnO nanoparticles to selected environmentally relevant test organisms and mammalian cells in vitro: a critical review", *Arch Toxicol*, t. 87, nr 7, s. 1181–1200, lip. 2013, doi: 10.1007/s00204-013-1079-4.

[61] ISO 22196:2011 International Organization for Standardization, „Measurement of antibacterial activity on plastics and other non-porous surfaces", International Organization for Standardization, Geneva, International Standard ISO 22196:2011, 2011.

[62] ISO 21702:2019 International Organization for Standardization, „Measurement of antiviral activity on plastics and other non-porous surfaces", International Organization for Standardization, Geneva, International Standard ISO 21702:2019, 2019.

[63] No 528/2012 European Parliament and Council, „Regulation (EU) No 528/2012 concerning the making available on the market and use of biocidal products", 2012.